Mediterranean Marine Science

Vol 20, No 4 (2019)

special issue

Numerical and experimental studies of a multi-purpose floating TLP structure for combined wind and wave energy exploitation

THOMAS MAZARAKOS, DIMITRIOS KONISPOLIATIS, GEORGIOS KATSAOUNIS, STYLIANOS POLYZOS, DIMITRIOS MANOLAS, SPYROS VOUTSINAS, TAKVOR SOUKISSIAN, SPYRIDON A. MAVRAKOS

doi: 10.12681/mms.19366

Research Article

Mediterranean Marine Science
Indexed in WoS (Web of Science, ISI Thomson) and SCOPUS
The journal is available on line at http://www.medit-mar-sc.net
DOI: http://dx.doi.org/10.12681/mms.19366

This paper was presented at *"12th Panhellenic Symposium of Oceanography & Fisheries"*, which was held at the Ionian University, Corfu, from 30th May to 3rd June 2018

Numerical and experimental studies of a multi-purpose floating TLP structure for combined wind and wave energy exploitation

Thomas MAZARAKOS[1] , Dimitrios KONISPOLIATIS[1] , Georgios KATSAOUNIS[2], Stylianos POLYZOS[2], Dimitrios MANOLAS[3], Spyros VOUTSINAS[3], Takvor SOUKISSIAN[4] and Spyros MAVRAKOS[1,4]

[1] Laboratory for Floating Structures and Mooring Systems, School of Naval Architecture and Marine Engineering, National Technical University of Athens, 9 Heroon Polytechniou Avenue, GR 157-73 Athens, Greece
[2] Laboratory for Ship and Marine Hydrodynamics, School of Naval Architecture and Marine Engineering, National Technical University of Athens, 9 Heroon Polytechniou Avenue, GR 157-73 Athens, Greece
[3] Laboratory of Aerodynamics, School of Mechanical Engineering, National Technical University of Athens, 9 Heroon Polytechniou Avenue, GR 157-73 Athens, Greece
[4] Hellenic Centre for Marine Research, Institute of Oceanography, Anavyssos, Greece

Corresponding author: tmazarakos@naval.ntua.gr

Handling Editor: Christos ARVANITIDIS

Received: 17 December 2018; Accepted: 4 November 2019; Published on line: 20 December 2019

Abstract

This paper summarizes the coupled hydro-aero-elastic analysis of a multi-purpose floating structure suitable for offshore wind and wave energy exploitation. The analysis incorporates solutions for the diffraction and the pressure- and motion- dependent radiation problems around the floating structure and the aerodynamics of a 5 MW Wind Turbine (WT). Finite water depths are considered, given that the structure floats under the action of regular surface waves. The platform encompasses three hydrodynamically interacting Oscillating Water Column (OWC) devices consisting of concentric vertical cylinders, moored using tensioned tethers in a TLP concept. Details concerning the numerical and experimental modelling of the system are presented and the numerical results are compared against experimental data.

Keywords: Wind Turbine; Oscillating Water Column; TLP; Numerical Calculations; Experiments.

Introduction

The main challenge in offshore energy exploitation is to build a structure capable to withstand the challenging environmental conditions, while being financially competitive compared with other types of energy converters. Among the numerous concepts for wave energy conversion, one promising alternative is the multi body floating structure equipped with wave energy converters based on the OWC principle. Konispoliatis & Mavrakos, (2016) and Konispoliatis *et al.,* (2016) have focused mainly on wave energy exploitation, while Aubault *et al.* (2011), Mazarakos *et al.,* (2014) and Mazarakos *et al.* (2017) have presented a numerical and experimental analysis of the combined exploitation of wind and wave energy sources for renewable electricity generation. Such multi-purpose floating platforms may represent a cost-effective engineering solution that increase the anticipated energy extraction to production cost ratio, as compared to isolated offshore wind or wave energy power plants. As wind and wave energy converters share common infrastructure (floater, electrical cable and power transfer equipment), the installation of several devices on a single floating hub has economic and operational advantages.

To design cost effective multi-purpose floating structures with structural and dynamic integrity and reliability, an integrated load analysis should be performed, following proper site assessment that would determine the design environmental conditions. The latter are evaluated using conditional statistical analysis of extremes, while the integrated load analysis is conducted using numerical aero-hydro-servo-elastic simulation tools (Riziotis & Voutsinas, 1997, Manolas, Riziotis & Voutsinas, 2014) combined with the hydrodynamic modelling of the floater through analytical methods or panel methodologies that account for the hydrodynamic interactions among

adjacent OWCs (Mavrakos & McIver, 1997; Kagemoto & Yue, 1986; Delaure & Lewis, 2003; Sykes *et al.,* 2007; Siddorn & Eatock Taylor, 2008; Konispoliatis *et al.,* 2016).

An analysis of the wind and wave climate at the candidate installation locations is necessary in order to realistically model the environmental conditions under which the structure will operate (see Soukissian & Chronis, 2000; Soukissian *et al.,* 2002, Soukissian *et al.,* 2017). In the same context, an estimate of the extreme environmental conditions is most important for the safety and operability of the structure (Soukissian & Kalantzi, 2006, 2007; Soukissian & Tsalis, 2015, 2018). In this work, design values were estimated by implementing a suitable bivariate model for the description of the wind speed and wave height and thus a joint description of their extreme values (Cheng *et al.,* 2003; Baarholm *et al.,* 2010; Yang & Chang, 2013; Li *et al.,* 2013).

In order to consistently take into account the contribution of the WT to the dynamic equations of a floater's motion, a reduced order design tool is used, which is based on Hamiltonian dynamics and Blade Element Momentum theory. It estimates the additional mass, damping and stiffness terms that are part of the inertial (including gyroscopic), gravity and aerodynamic loading of the WT, and estimation of 6-degree-of-freedom (dofs) for the floater.

As far as the hydrodynamic analysis of the proposed floater is concerned, the in-house developed computer code HAMVAB (Hydrodynamic Analysis of Multiple Vertical Axisymmetric Bodies; Mavrakos, 1995) software was used. This software, which relies on analytical representations of the velocity potential around each cylinder-type device of the array, was preferred for the current study against other available numerical tools applicable to general 3-D geometries, in order to reduce the computational cost while keeping the same accuracy (Konispoliatis & Mavrakos, 2016; Mavrakos & Koumoutsakos, 1987). Hence, it represents an efficient alternative tool in the early design phases of such type of floating structures.

To further examine the behaviour of such multi-purpose floating structures, an extensive set of experiments was conducted on a scaled-down model of the platform. The scientific aim of the tests was to provide data for the validation of the numerical analysis of the platform; the mooring components; the WT loads on the floater and the OWC characteristics, i.e. the pressure difference (drop) between the air chamber and the outside space and the volumetric flow rate, passing through the air turbine of the device. The experimental set up and details of the experiments and corresponding experimental results have been presented by Katsaounis *et al.* (2017)**.**

The main objective of the current study, which can be considered as a follow up and enhancement of the previous works of Mazarakos *et al.,* (2017) and Katsaounis *et al.* (2017), is to present, in a systematic way, a frequency-domain analysis approach along with its experimental verification for the coupled hydro- aero- elastic analysis of a multi-purpose floating structure suitable for the exploitation of offshore wind and wave energy sources. The method is an effective design tool for the analysis of floating wind turbines and multi-purpose floating solutions at the first stages of their development, offering a fast analysis methodology for the investigation of alternative design concepts. The manuscript is structured as follows: first the wave and wind climate analysis for four selected locations in the Greek seas is presented in order to define design environmental parameters (wind and wave); then follows the design of the floating multi-purpose system for combined wind and wave energy conversion, its hydrodynamic analysis and the definitions of the TLP mooring system. The next step of the analysis is the formulation of the aero-elasto-dynamic problem due to the WT, and the solution of the coupled hydro- aero-elastic problem of the floating supporting structure -WT-OWC-and mooring system. The final step consists in a detailed presentation of the experiments conducted for evaluating the hydrodynamic behaviour of the floating structure and comparing with numerical results.

Applied Methodologies & System Description

Environmental Conditions and Design Values

Wind and wave climate analysis has been performed for four selected locations of the Greek Seas. The hindcast wind and wave data used in the analysis were obtained from the Eta-based numerical weather prediction model of the POSEIDON system, **see** Papadopoulos & Katsafados (2009)**,** Papadopoulos *et al.* (2011) and the WAM wave model, and cover the 10-year period 1/1/1995 – 31/12/2004. The results are provided every three hours (00:00, 03:00, 06:00, 09:00, 12:00, 15:00, 18:00, 21:00, and 24:00 UTC). An analytic description of the wind and wave hindcast data is provided in Soukissian *et al.* (2008)**.** The particular locations examined are shown in Table 1; see also Figure 1**.** In Table 2, the basic statistical characteristics (mean value *m*, minimum *min*, and maximum *max*, standard deviation *s*, coefficient of variation *CV* skewness *Sk* and kurtosis *KU* coefficients, along with the available sample size *N*) are summarized for the significant wave height H_S, spectral peak period T_p and wind speed V_W.

As shown in Table 2, the most intense sea-state and wind conditions are encountered at location A4 (mean and overall maximum significant wave height 1.03 m and 7.14 m, respectively, and mean wind speed 6.47 m/s). The overall maximum wind speed occurs at A2 (23.89 m/s). The largest variability is exhibited for significant wave height at A3 (92.28%) and the minimum for spectral peak period at A4 (28.24%).

Extreme value analysis and estimation of joint design values

The estimation of bivariate design values for metocean parameters is an open theoretical study field. Unlike the extreme value theory of 1-D random variables,

Table 1. Examined Locations of the Greek Seas.

			Bottom depth
A1	35.76° N	23.34° E	~200 m
A2	38.61° N	24.21° E	~60 m
A3	39.96° N	24.97° E	~200 m
A4	35.43° N	26.81° E	~200 m

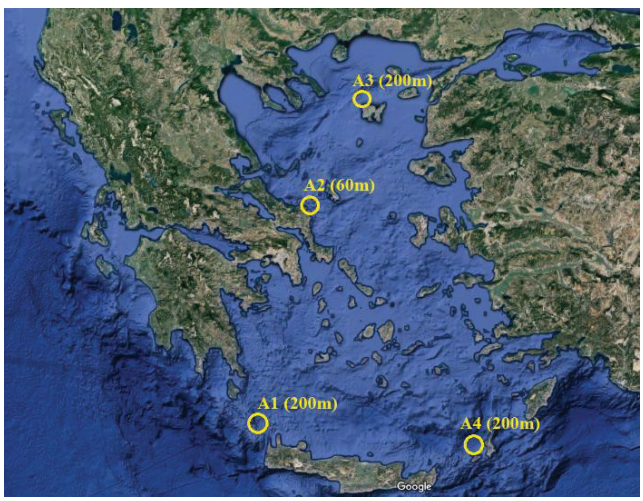

Fig. 1: Examined locations at the Aegean Sea (Google Map).

the multivariate extreme value theory has some important theoretical difficulties that have not been overcome. In the ocean engineering community, some alternative and simplified methods for the estimation of joint design values have been proposed. These methods adopt some important assumptions, but in practice it seems to work quite satisfactorily (Cheng *et al.,* 2003; Baarholm *et al.,* 2010; Yang & Chang, 2013; Li *et al.,* 2013). The most remarkable of these methods is based on the implementation of the Rosenblatt transformation and will be used in this work for the estimation of the joint design values of significant wave height- wind speed and significant wave height- spectral peak wave period.

In this respect and taking the case of H_S and V_W, as an example, let $f_{H,V}(h_S, v_H)$ denote the joint probability density function (pdf) of H_S and V_W. Using the total probability theorem, $f_{H,V}(h_S,v_W)$ can be written as follows:

$$f_{H,V}(h_S, v_W) = f_V(v_W) f_{H|V}(h_S|v_W) \qquad (1)$$

where $f_{H|V}(h_S|v_W)$ is the conditional pdf of significant wave height given wind speed.

Using the Rosenblatt transformation, see Rosenblatt (1952), the random variables H_S, V_W can be transformed into the corresponding Gaussian and uncorrelated variables, u_1, u_2 respectively. The Rosenblatt transformation is of the following form:

$$F_V(v) = \Phi(u_1), \qquad F_{H|V}(h|v) = \Phi(u_2) \qquad (2)$$

where $\Phi(\cdot)$ is the standardized Gaussian distribution (with zero mean value and standard deviation 1). For the estimation of u_1 and u_2 the inverse of the above equations are used:

$$u_1 = \Phi^{-1}\big(F_V(v)\big), \qquad u_2 = \Phi^{-1}\Big(F_{H|V=v}(h|v)\Big) \quad (3)$$

Variable u_1 reflects the marginal variability of V_w and u_2 the conditional variability of $H_S|V_W$. This implies that in order to apply the Rosenblatt transformation, the entire domain of definition of the random variables V_W and $H_S|V_W$ should be considered.

To return to the original variables H_S and V_W the following relations should be used:

$$v = F_V^{-1}\big(\Phi(u_1)\big), \qquad h = F_{H|V=v}^{-1}\big(\Phi(u_2)\big) \quad (4)$$

Let us note that the procedure described above is structured in such a way so as to reflect more reliably the high values of H_S - V_W and H_S - T_P. After the generation of the corresponding samples from the random variables u_1 and u_2, the sample space can be represented in the u_1-u_2 plane, where the RP years return period can be defined as a circle of radius r that is given by the following relationship:

Table 2. Basic statistical characteristics of wind and wave time series in the examined locations.

		N	*m*	min	max	*s*	*CV*	*Sk*	*Ku*
H_S (m)	A1	29218	0.98	0.10	6.40	0.61	62.02	1.71	4.19
	A2		0.62	0.01	5.94	0.50	82.21	2.42	9.28
	A3		0.54	0.00	5.08	0.49	92.28	2.48	8.81
	A4		1.03	0.09	7.14	0.62	60.87	1.78	5.73
T_p (s)	A1		5.57	1.68	15.03	1.65	29.62	0.89	0.80
	A2		3.97	1.26	10.26	1.40	35.11	1.36	2.02
	A3		3.64	1.26	9.33	1.23	33.69	1.22	1.67
	A4		5.38	1.68	13.66	1.52	28.24	1.05	1.59
V_W (m/s)	A1		5.78	0.19	19.00	2.90	50.21	0.61	-0.13
	A2		5.34	0.06	23.89	3.09	57.85	0.54	-0.08
	A3		4.85	0.09	21.62	3.05	62.85	1.05	1.18
	A4		6.47	0.11	20.57	3.33	51.53	0.35	-0.34

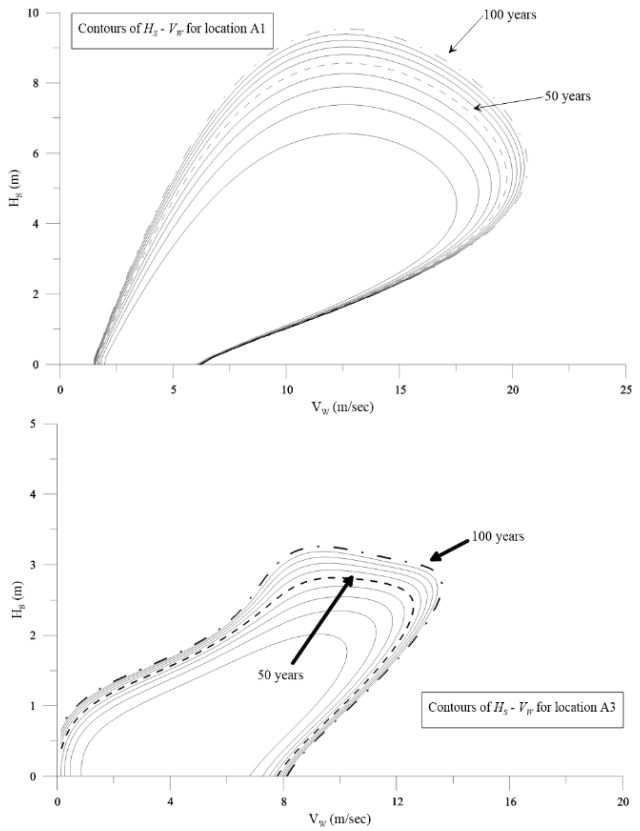

Fig. 2: Contours of H_S and V_W for locations A1 (first row) and A3 (second row).

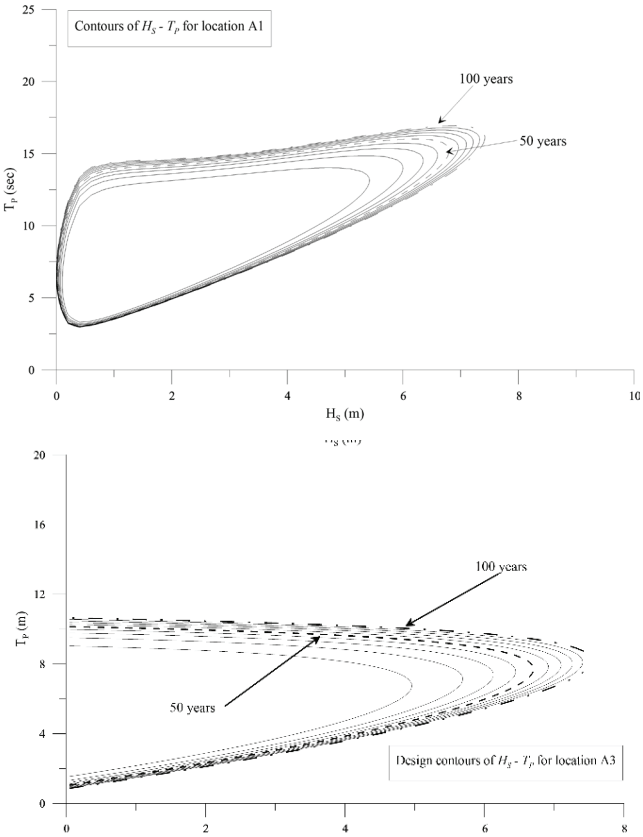

Fig. 3: Contours of and for locations A1 (first row) and A3 (second row).

$$\Phi(r) = 1 - \frac{1}{N_{RP}} \qquad (5)$$

where N_{RP} is the number of sea states expected to appear in RP years. Here it is assumed that the sea-state duration is constantly equal to the recording interval of the initial data series. For a recording interval (R1) of 3 hours N_{RP} is given as follows:

$$N_{RP} = 365.25\ (days/year) \times 8\ (observ./day) \times RP(years) \qquad (6)$$

The generalization of the above procedure in the 3-D case is immediate; however, in this case the computational cost is high.

Some indicative results obtained by implementing the above procedure are shown in Figure 2 (for H_S and V_W) and Figure 3 (for H_S and T_P).

Description of the Floating Platform

The examined floating system has been proposed for the NREL 5MW WT, which is a variable-speed variable-pitch controlled WT. The tower of the wind turbine is cantilevered at an elevation of 10m above the sea water level (SWL) to the top of the central column of a floating triangular platform (Fig. 4).

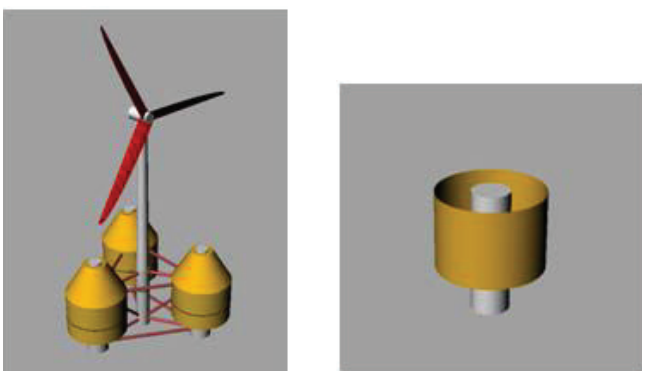

Fig. 4: 3-D representation of the floating platform and of each device's oscillation chamber.

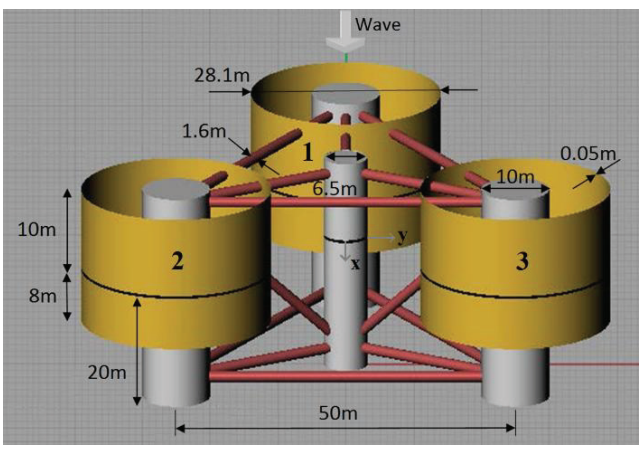

Fig. 5: Side view of the buoyant components.

Table 3. Floating Platform Geometry.

Depth of platform base below SWL (total draft)	20m
Elevation of main column (tower base) above SWL	10m
Elevation of offset columns above SWL	10m
Spacing between columns	50m
Draft of the structure	20m
Diameter of main column	6.5m
Diameter of inner concentric cylindrical body	10m
Outer radius of the OWC chamber on each device	14m
Outer radius of the OWC chamber on each device	14.05m
Oscillating chamber's draught	8m
Diameter of brackets and cross braces	1.6m

Table 4. Mass Distribution.

Mass of the floater	2183.6 t
Mass of the 5 MW WT	600 t
Mass of the Wells turbine (including generator)	3 t
Total mass of the platform	2827.6 t
CM location below SWL	4.05 m
Centre of Buoyancy below SWL	9.90 m
Platform roll inertia about CM	1.106E6 tm^2
Platform pitch inertia about CM	1.106E6 tm^2
Platform yaw inertia about CM	1.987E6 tm^2

A system of three identical OWC devices consisting of concentric vertical cylinders that are mounted at the corners of a triangular floater and can oscillate about their mean equilibrium position moving as a unit are considered (Fig. 5). A regular monochromatic wave was propagating along the positive x-axis (Fig. 5) causing the captured water column to oscillate in the annular chamber, compressing and decompressing the air above the inner water surface. As a result, there is an air flow moving forwards and backwards through a turbine coupled to an electric generator. A summary of the geometry, including the diameters of each of the parts of the structure is given in Table 3. These properties are all relative to the un-displaced position of the platform.

The mass, including ballast, of the floating platform is 2183.6 t. This mass was calculated so that the combined weight of the rotor-nacelle assembly, tower, platform, plus the applied TLP pretension and the weight of the mooring system in water, balances with the buoyancy (i.e. weight of the displaced fluid) of the platform in the static equilibrium position in still water. The centre of mass (CM) of the floating platform, including ballast, is located at 4.05 m along the platform centre line below the SWL. The roll and pitch inertias of the floating platform about its CM are 1.106E6 tm^2 and 1.106E6 tm^2 about the platform x-axis and y-axis respectively, while the yaw inertia of the floating platform about its Centre line is 1.987E6 tm^2 (Table 4).

Formulation of the Hydrodynamic Problem

Multi Body Velocity Potential Representation

The detailed potential theory of the hydrodynamic problem of an array of OWC devices has been extensively reported in the literature (Konispoliatis & Mavrakos, 2016; Konispoliatis *et al.,* 2016). For completeness, a sort introduction to the theory is provided.

The group of the 4 bodies (3 OWC devices and 1 vertical cylindrical body supporting the WT) is excited by a plane periodic wave of amplitude $H/2$, frequency ω and wave number k propagating in water of finite water depth d (i.e. 120 m). The outer and inner radii of each device's chamber q, q=1,2,3 are denoted by a_q, b_q respectively (i.e. $a_q = 14.05m$; $b_q = 14$m; $q = 1,2,3$). The radius of the interior concentric cylindrical body in each device q, and the radius of the central vertical cylindrical body supporting the WT are denoted by $b_{l,q}$ and c, respectively (i.e $b_{l,q} = 5m$; $q = 1,2,3$; $c = 3.25m$).

The fluid is assumed non viscous and incompressible and the flow irrotational, so that the linear potential theory can be used. A global Cartesian co-ordinate system O-XYZ with origin on the sea bed and its vertical axis OZ directed positive upwards is used. Moreover, three local cylindrical co-ordinate systems (r_q, θ_q, z_q) q = 1,2,3 are defined with origins on the sea bottom and their vertical axes pointing upwards. The velocity potential around the q = 1,2,3,4 device / body (three OWCs at the vertices of the triangular floater and the vertical central cylindrical body that supports the WT), $\Phi^q(r_q, \theta_q, z_q; t) = Re[\varphi^q(r_q, \theta_q, z_q) \cdot e^{-i\omega t}]$ can be decomposed into a form (Falnes & McIver, 1985):

$$\varphi^q = \varphi_0^q + \varphi_7^q + \sum_{p=1}^{4}\sum_{j=1}^{6} \dot{\xi}_{j0}^p \cdot \varphi_j^{qp} + \sum_{p=1}^{3} p_{in0}^p \cdot \varphi_P^{qp} \quad (7)$$

Here, φ_0^q is the velocity potential of the incoming undisturbed incident harmonic wave; φ_7^q is the scattered potential around the q device; φ_j^{qp} is the motion-dependent radiation potential around the body q resulting from the forced oscillation of the p body in j direction with unit velocity amplitude, $\dot{\xi}_{j0}^p$, (j = 1,2, ..., 6) φ_j^{qp} is the pressure-dependent radiation potential around the q body due to unit time harmonic oscillating pressure head, $P_{in}^p = Re[p_{in0}^p \cdot e^{-i\omega t}]$, in the chamber of the p device (Konispoliatis *et al.,* 2016). It holds $\dot{\xi}_j^p = Re[\dot{\xi}_{j0}^p \cdot e^{-i\omega t}] = Re[-i\omega\xi_{j0}^p \cdot e^{-i\omega t}]$ and the subscript j stands for surge (j = 1), sway (j = 2), heave (j = 3), roll (j = 4), pitch (j = 5) and yaw (j = 6) modes of motions, respectively.

The potentials φ_j^q (j= 0, 7; q = 1, 2, 3, 4), φ_j^{qp} (j= 1, …, 6; q, p = 1, 2, 3, 4) and φ_j^{qp} (q = 1, 2, 3, 4; p = 1, 2, 3) are solutions of Laplace's equation in the entire fluid do-

main and satisfy the following boundary conditions:

$$\omega^2\varphi_j^{qp} - g\frac{\partial\varphi_j^{qp}}{\partial z} = \begin{cases} 0 & \text{for } r_q \geq a_q; r_q \geq c; j = 0{,}7; i = q \\ 0 & \text{for } r_q \geq a_q; r_q \geq c; j = 1,..,6, P; i = qp \\ 0 & \text{for } b_{1,q} \leq r_q \leq b_q; j = 1,..,6, P; i = qp \\ -\delta_{q,p}\frac{i\omega}{\rho} & \text{for } b_{1,q} \leq r_q \leq b_q; j = P; i = qp \end{cases} \quad (8)$$

at the outer and inner free sea surface $z=d$ of each body, and the zero normal velocity on the sea bed (z=0). Furthermore, the potentials have to fulfil kinematic conditions on the mean body's wetted surface (Konispoliatis & Mavrakos, 2016). Finally, a radiation condition must be imposed which states that propagating disturbances must be outgoing.

The unknown potential functions involved in Eq. (7) can be established throughout the method of matched axisymmetric eigenfunction expansions by subdividing the flow field around each device/body in coaxial ring shaped fluid regions. In each of those regions different series expansions of the velocity potentials are derived. These are solutions of the Laplace equation in each fluid region and are selected so that the kinematic boundary condition at the horizontal walls of the device/body, the linearized condition on the free surface, the kinematic condition on the sea bottom and the radiation condition at infinity are satisfied. The various potential solutions are then matched by continuity requirements of the hydrodynamic pressure and radial velocity along the vertical boundaries of adjacent fluid regions, as well as by fulfilling the kinematic conditions at the vertical walls of the device/body. The method has been extensively described in the past (Miles & Gilbert, 1968; Garrett, 1971; Black *et al.,* 1971; Kokkinowrachos *et al.,* 1987; Mavrakos & Konispoliatis, 2012) and, therefore, it is not further elaborated here.

The hydrodynamic interaction phenomena among the members of the multi-body configuration have been taken into account through the physical idea of multiple scattering (Twersky, 1952; Okhusu, 1974; Mavrakos & Koumoutsakos, 1987; Mavrakos, 1991). By properly superposing the incident wave potential and the propagating and evanescent modes that are scattered and radiated by the array elements, exact representations of the total wave field around each body of the array can be obtained. This method is detailed in (Konispoliatis & Mavrakos, 2016) to solve the diffraction, the motion- and the pressure- dependent radiation problems for an interacting array of OWC's devices.

Volume Flow

Having determined the velocity potentials in all fluid domains, the time dependent volume flow $Q^q(t) = Re[q^q \cdot e^{-i\omega t}]$ produced by the oscillating internal water surface in the q device (q=1,2,3) is denoted by:

$$q^q = \iint_{S_i^q} \frac{\partial\varphi^q}{\partial z} r_q dr_q d\theta_q \quad (9)$$

Here S_i^q is the cross-sectional area of the inner water surface inside the q device.

We assume that in all the OWC devices a Wells turbine is installed in order to convert the energy of the air flow into electricity. This is a bidirectional turbine, designed for directional changing air flows, like the ones produced in the air chamber of the OWC under the action of the oscillating water surface, due to wave action. The turbine is represented by a pneumatic complex admittance Λ; thus, the total volume flow, q^q in the q device (q=1,2,3) is related to the corresponding inner air pressure by (Falcao, 2002; Martins-rivas & Mei, 2009):

$$p_{in0}^p = \Lambda \cdot q^q = \left(\frac{KD}{N\rho_{air}^0} - i\omega\frac{V_0^q}{c_{air}^2\rho_{air}^0}\right)^{-1} \cdot q^p \quad (10)$$

Here N is the rotational speed of turbine blades, D the outer diameter of turbine rotor, ρ_{air}^0 the static air density V_0^q the q device's air chamber volume and c_{air} being the sound velocity in air. The empirical coefficient K depends on the design, the setup and the number of turbines. For the sake of validation of the numerical results with the experimental ones, the air compressibility is neglected in this study and, thus, the pneumatic admittance Λ is considered to be a real number.

Following Evans & Porter (1996), when the pneumatic admittance Λ of an OWC restrained in the wave impact and in isolation condition equals an optimum coefficient Λ_{opt}, the absorbed power by the OWC device reaches its maximum value (see also Konispoliatis *et al.,* 2016).

Mooring System

To secure the platform, the floating system is moored with a TLP mooring system consisting of three tendons spread symmetrically around the platform Z-axis. The fairleads (body-fixed locations where the mooring tendons attach to the platform) are located at the base of the offset columns, at a depth of 20m below the SWL. The anchors (fixed to the inertia frame) are located at a water depth of 120m below the SWL. Each of the 3 tendons has an unstretched length of 100m. The mooring forces, $f_{i,moor}$ acting on the platform in the i-th direction can be derived from:

$$f_{i,moor} = C_{i,j,mooring} \cdot \xi_{j0}; \; i,j = 1,...,6 \quad (11)$$

Here, ξ_{j0} is the motion component of the entire system at the j-th direction with respect to the global co-ordinate system G, of the platform's motions and $Ci,j,mooring$ is the platform's mooring line stiffness matrix defined by:

$$C_{1,1,mooring} = C_{2,2,mooring} = \sum_{n=1}^{3} \frac{T_n}{L}$$
$$C_{3,3,mooring} = \frac{EA}{L} \quad (12)$$

Here, T_n are tendon pretension forces; A is the total cross-section area and L is the tendon's length (i.e. L=100m).

Each tendon has a diameter of 0.130 m, an equivalent mass per unit length of 104 kg/m, an equivalent apparent mass in fluid per unit length of 888.6 N/m and a pretension value of 10800 kN.

The TLP increases the vertical stiffness of the floating system, which reduces the heave period. In this way, the heave period can be shifted out of the high-energy region of the sea spectrum. From a static stability point of view, this pretension can be considered as a point mass located at the connection point of the tension leg. In addition to the resulting downward shift of the virtual centre of gravity, the centre of buoyancy is also moved downward in absolute sense since additional buoyancy is required to compensate the pretension. The mooring tendon properties are listed in Table 5.

Table 5. Mooring System properties.

Number of Tendons	3
Depth to Anchors Below SWL (Water Depth)	120m
Depth to Fairleads Below SWL	20
Mooring Line Length	100m
Mooring Line Diameter	130m
Equivalent Mooring Line Mass Density	104kg/m
Equivalent Mooring Line Mass in Water	888.6N/m
Mooring Line stiffness k_{xx} of each tendon	108.0 kN/m
Mooring Line stiffness k_{ZZ} of each tendon	26533 kN/m
Pretension of each tendon	10800 kN

Coupled Motion Equation

The motion equations that govern the linear dynamic motions of the system are summarized in matrix form (Mazarakos *et al.,* 2014; 2015; Konispoliatis *et al.,* 2016):

$$\sum_{j=1}^{6}\left[-\omega^2\left(M_{i,j}+M_{i,j}^{WT}+A_{i,j}+\frac{i}{\omega}B_{i,j}+\right.\right.$$
$$\left.\left.+\frac{i}{\omega}B_{i,j}^{WT}\right)+C_{i,j}+C_{i,j,mooring}+C_{i,j}^{WT}\right]\cdot\xi_{j0}-$$
$$-f_p^T=f_i^T,\ i=1,2,\ldots,6 \quad (13)$$

The superscript *WT* corresponds to the physical quantities associated with the wind turbine. Moreover, $C_{i,j}$ and C_i are elements of the mass and stiffness matrix of the floating structure, $A_{i,j}$, $B_{i,j}$ and $C_{i,j,mooring}$ represent its 6 by 6 added mass, damping, and mooring line stiffness matrices, respectively. f_i^T, and f_p^T are the six by one vectors that contain the hydrodynamic exciting forces and the pressure hydrodynamic forces on each floating supporting structure, respectively and ξ_{j0} is the motion displacement of the entire system at the j-th direction with respect to the global co-ordinate system G. $M_{i,j}^{WT}$, $B_{i,j}^{WT}$ and $C_{i,j}^{WT}$ are the mass, damping and stiffness which contribute to the WT's aerodynamic, inertial-gyroscopic and gravitational loading, respectively (see next first order section).

Shear Forces

To calculate the shear forces and bending moments, the following analysis can be made.

The response of local motion is calculated as in Eq. (13). To calculate the displacement of the structure along an intersection point r=(x,y,z), the local motion of each body should be calculated (Mazarakos *et al.,* 2018).

$$s_1=\xi_1+z\xi_5-y\xi_6$$
$$s_2=\xi_2+x\xi_6-z\xi_4$$
$$s_3=\xi_3+y\xi_4-x\xi_5 \quad (14)$$
$$s_4=\xi_4$$
$$s_5=\xi_5$$
$$s_6=\xi_6$$

The shear forces along an intersection point $\boldsymbol{r}$=(x,y,z), is the sum of the forces acting at each body of the configuration, $\boldsymbol{F}_i$=(F_{xi}, F_{yi}, F_{zi}), i=1,2 (where 1=Floating Structure, 2=Wind Turbine), (Fig. 6).

The bending moment along an intersection point r=(x,y,z), is the sum of the moments acting at each body of the configuration, $\boldsymbol{M}_i$=(M_{xi}, M_{yi}, M_{zi}), where i=1,… number of elements, plus the cross product of the force exerted on each body of the configuration at its distance from the point of intersection:

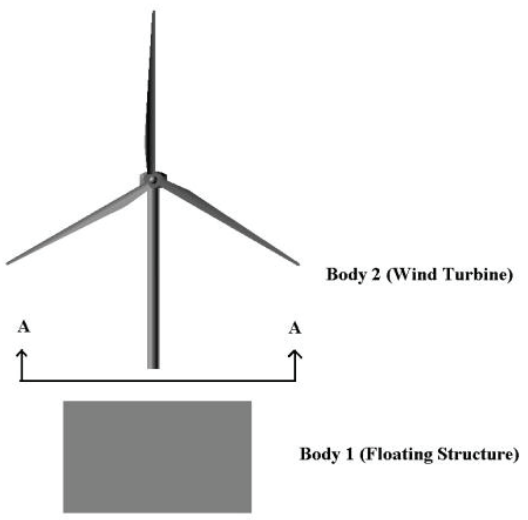

Fig. 6: Sketch of the intersection point for the shear forces calculations.

$\boldsymbol{M}_{\text{int}}=\boldsymbol{r}\boldsymbol{x}\boldsymbol{F}_i+\boldsymbol{M}_i$:

$$M_{int} = (yF_{zi} - zF_{yi} + M_{xi}, zF_{xi} - xF_{zi} + M_{yi}, xF_{yi} - yF_{xi} + M_{zi}) \quad (15)$$

Formulation of the Aero-elasto-dynamic Problem

The problem is formulated in the context of Hamiltonian dynamics. External loading includes aerodynamic loading on the rotor, inertial loading due to the rotation of the blades and the motions of the floater, as well as gravitational loading and hydrostatic loading on the floater. Aerodynamic loading is defined within the context of Blade Element Momentum theory and implemented through the modules of RAFT (which is one of the two aerodynamic modules in hGAST (Riziotis & Voutsinas, 1997; Manolas, Riziotis & Voutsinas, 2014).

Model formulation

In Hamiltonian dynamics, the behaviour of mechanical systems is described by the Lagrange equations. To this end, appropriate generalized co-ordinates or dofs q_j are defined that describe the position of any material point r. Based on the definition of the position, the kinetic energy is readily obtained. Depending on the assumptions made regarding the flexibility of the system, the definition of the position also includes dofs that describe the motions of the components due to their flexibility and, therefore, the potential or internal energy can be defined. Finally, the external loading is introduced through the virtual work contributed by this loading. The equations have the following form:

$$\frac{d}{dt}\left(\frac{\partial L}{\partial \dot{q}_j}\right) - \left(\frac{\partial L}{\partial q_j}\right) = Q_j = \sum_i \frac{\partial (\boldsymbol{f}_i \cdot \boldsymbol{r}_i)}{\partial q_j} \quad (16)$$

where $L=T-U$ denotes the Lagrangian of the system, T its kinetic energy, U its potential or internal energy and Q_j the generalized loads corresponding to the external loads f_i (assumed as concentrated forces and moments).

In the proposed formulation, dofs are introduced for all components: 2 rotation dofs per blade at the root that correspond to the 2 bending directions, 1 dof for the torsion deformation and 1 dof for the rigid body rotation of the drive train; 3 dofs at the tower base, 2 for bending and 1 for torsion in yaw; 6 dofs in total for the floater motions, 3 translational and 3 rotational.

Aerodynamic modelling

In Blade Element Momentum theory, the aerodynamic forces along the blade span, are obtained by solving the following two nonlinear equations for the induction factors a and a' that specify the effective angle of attack α and the effective relative velocity U_{eff}.

$$N(C_L(\alpha)cos\varphi + C_D(\alpha)sin\varphi)c = \frac{8\pi U_W^2}{U_{eff}^2}\mathrm{a}(1-\mathrm{a})r$$

$$N(C_L(\alpha)sin\varphi - C_D(\alpha)cos\varphi)c = \frac{8\pi U_W \Omega r}{U_{eff}^2}\,\mathrm{a}'(1-\mathrm{a})r \quad (17)$$

In the above equations N denotes the number of blades, C_L and C_D the lift and drag coefficients provided in tabulated form as a function of the effective angle of attack, U_W the magnitude of the undisturbed wind velocity, φ the angle between the effective velocity and the rotor plane, r the radial position of each blade element, c the local chord length and Ω the rotational speed.

The effective speed U_{eff} and the angle φ are defined as (see Fig. 7),

$$U_{eff} = \sqrt{(U_W(1-\mathrm{a}))^2 + (\Omega r(1+\mathrm{a}'))^2} \quad (18)$$

$$tan\varphi = \frac{U_W(1-\mathrm{a})+\delta u_a}{\Omega r(1+\mathrm{a}')+\delta u_c} \quad (19)$$

while the angle of attack α which is needed in order to define the C_L, C_D data is defined as,

$$\alpha = \varphi - (\theta_t + \beta_p) \quad (20)$$

where θ_t and θ_p denote the local twist and blade pitch angle respectively.

In Eq. (19), δu_a and δu_c correspond to any extra velocity contribution in the axial and circumferential direction, respectively. Such contributions derive from the deformation velocities but also from the rigid body motions (i.e. the motions of the floater).

Once the iterative process for the solution of the nonlinear system of Eq. (17) converges, the lift (L) and drag (D) force along the blade span are calculated as,

$$F_*(r,a) = 0.5\,\rho_{air}\,C_*(r,\alpha)U_{eff}^2 c dr, \quad *= L, D \quad (21)$$

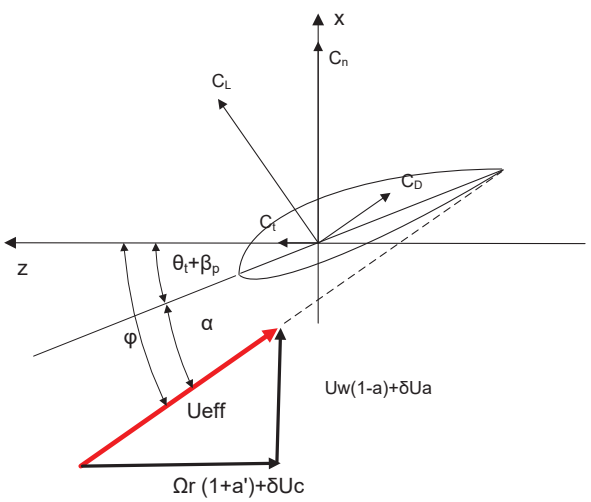

Fig. 7: The rotor flow characteristics based on blade element momentum theory.

where ρ_{air} denotes the air density and *dr* the length of the annulus tube per blade element strip.

The equations for a, a' are nonlinear by definition and should be solved together with the rest of the dynamic equations, namely, the structural equations of the complete system and the motion equations of the floater. It is however possible to linearize the problem by assuming a given reference state with respect to which all additional perturbations are considered small, and to eliminate part of the problem by assuming that all relevant dofs are fixed (i.e. the elastic dofs of the WT).

Dynamic definition of the mechanical system

For the mechanical system corresponding to a wind turbine, the following approach is followed:

The system is composed of a number of components, such as the blades, the drive train, the tower, the floater and the mooring lines.

Each component is considered at most as a 1-D structure either modelled as rigid or as a flexible beam undergoing bending, tension and torsion. Mass as well as structural properties can be locally integrated, and concentrated properties are defined. For example, the blade can be considered as a point mass placed at the mass centre of the blade. Concentrated properties are important for simplified modelling. However, care should be taken so that the dynamics introduced by concentrated properties are equivalent to those of the full distributed system. This, for example, entails that a point mass is associated with a full 6x6 mass matrix. Similarly, structural properties can be concentrated in the form of linear or rotation springs. In this case, equivalence should ensure accurate prediction of the first natural frequencies of the system.

A static solution can be defined by assuming that all components are rigid, the wind is uniform and steady, yaw misalignment and inclination are zero and the rotational speed and blade pitch are fixed (reference state for the controller). In this case, the position of the floater will be defined by the mass distribution of the system, the thrust and moment at the rotor hub, the buoyancy and the stiffness, which are associated with the 6 dofs of the floater. Among other, this static solution will correspond to a given aerodynamic loading distribution defined by a, a' and, therefore, a specific distribution of angles of attack.

In order to derive design equations for the floater, perturbations of the static solution are considered by keeping free only the 6 dofs q_{fl} of the floater, assuming the WT rigid (defining only its inertial characteristics). The ultimate aim is to keep only the equations for the sea level and below. Therefore, we keep the assumption of rigidity and add the further assumption that rotor aerodynamic induction is not affected by the floater motions. This means that a, a' will keep their static (reference) values and that the perturbation of the aerodynamic loads will only derive from the change in the angle of attack and the effective velocity through δu_a and δu_c. The linearized load takes the form:

$$Q = Q_0 + \partial_q Q_0 \cdot q_{fl} + \partial_{\dot{q}} Q_0 \cdot \dot{q}_{fl} + \partial_{\ddot{q}} Q_0 \cdot \ddot{q}_{fl} \quad (22)$$

In fact, the terms $\partial_* Q_0$ define the additional stiffness, damping and mass matrices in the floater equations. Note that $\partial_* Q_0$ depends on the static position of the floater as well as the reference operation conditions of the rotor (i.e. the wind speed, the rotational speed and the blade pitch).

Linearization process / derivation of WT matrices

Let $\alpha_0(r)$ denote the effective angle of attack for the reference state at a specific radial position *r*. For this angle, the lift and drag coefficients $C_{L0}(r)$, $C_{D0}(r)$ and their slope $\partial C_{L0}(r)$, $\partial C_{D0}(r)$ are obtained from the tabulated polar input. The linearization of lift and drag coefficient gives:

$$C_*(r,a) = C_{*0}(r) + \partial C_{*0}\, \delta\alpha, \quad *= L, D \quad (23)$$

where $\delta\alpha = \alpha - \alpha_0$ defines a (small) perturbation of the angle of attack due to the floater motion, so that $\delta\alpha(q_{fl}, \dot{q}_{fl})$. Linearization of $\delta\alpha(q_{fl}, \dot{q}_{fl})$ gives:

$$\delta\alpha(q_{fl}, \dot{q}_{fl}) = \overline{\delta\alpha_q} q_{fl} + \overline{\delta\alpha_{dq}} \dot{q}_{fl} \quad (24)$$

and similarly for the effective relative velocities δu_a and δu_c,

$$\delta u_*(q_{fl}, \dot{q}_{fl}) = \overline{\delta u_{*,q}} q_{fl} + \overline{\delta u_{*,dq}} \dot{q}_{fl,} \; *= a, c \quad (25)$$

By introducing the above expressions in Eq. (16) and eliminating higher order terms, the aerodynamic loading is projected on the floater dofs. Finally, by integrating along the blade span and applying Coleman's transformation (Coleman R.P., 1943), the loads are expressed in the coordinate system of the floater. The resulting dynamic equations are provided in the standard form, expressed for the 6 dofs of the floater:

$$M\ddot{q}_{fl} + B\dot{q}_{fl} + Cq_{fl} = Q \quad (26)$$

The right-hand side contains gravity, buoyancy as well as aerodynamics that correspond to the reference state. The mass, damping and stiffness matrices account for the WT inertia (including the gyroscopic effects due to rotation), the damping due to rotation and aerodynamics and the stiffness contribution from both aerodynamics and gravity respectively [terms $M_{i,j}^{WT}$, $B_{i,j}^{WT}$, $K_{i,j}^{WT}$ in Eq. (13)].

Wave Tank Experimental Analysis

Experimental Setup

A detailed presentation of the experimental campaign conducted for evaluating the hydrodynamic behaviour of the floating structure investigated in this paper, has been

presented by Katsaounis *et al.* (2017), with a short outline being presented here. Following the Froude's scaling law that is widely used for seakeeping tests, geometrical similarity against the real structure has been applied.

Taking into account the dimensions of the wave flume and the capacity of the wave maker, a 1:40 model scale was selected. The model is composed of three vertical cylinders at the corners of the triangular platform, forming the main buoyancy hull; a cylinder at the centre of the triangle supporting the wind turbine; horizontal and diagonal bracing elements; the cylindrical OWC chamber walls; the OWC air chamber conic domes; a wind turbine tower and tower base; a WT Nacelle assembly; a WT rotor; TLP tendons; and a bottom base for the tension leg connections.

Froude's law of similitude requires preservation of the following parameter (i.e. Froude number *Fn*):

$$Fn = \frac{\mathrm{U_{FS}}}{\sqrt{\mathrm{g\,L_{FS}}}} = \frac{\mathrm{U_M}}{\sqrt{\mathrm{g\,L_M}}} \tag{27}$$

where FS denotes the full scale, and M the model scale, U being a characteristic velocity (e.g. velocity of the platform motion or of the sea surface elevation due to waves), L a characteristic length and *g* the gravitational acceleration.

Froude's law of dynamic similarity (i.e. geometric similarity and similarity of forces) also preserves the ratio between the inertial and gravitational forces, since:

$$\frac{\text{Inertial Forces}}{\text{Forces due to gravity}} \propto \frac{\rho \mathrm{U^2 L^2}}{\rho\,\mathrm{gL^3}} = \frac{\mathrm{U^2}}{\mathrm{gL}} = \mathrm{Fn^2} \tag{28}$$

Thus, equality in *Fn* between model and full scale ensures the correct modelling of the gravitational forces and, consequently, of the surface wave forces, which are gravity-driven. Moreover, the inertial components of the loads are also correctly scaled, including the inertial loads of the wind turbine. To this end, and especially for modelling the gyroscopic loads due to the rotational momentum of the WT rotor, it should be noted that the WT rotation combined with the angular motion of the supporting platform produces a moment:

$$M^{gyr} = \omega I^R \Omega \tag{29}$$

where I^R is the angular moment of inertia of the rotor, ω is the angular velocity of the rotor and Ω is the angular velocity of the platform in yaw or pitch motion.

The relationship between the induced moments at model scale and full scale is:

$$M_M^{gyr} = M_{FS}^{gyr} \frac{1}{\lambda^4} \tag{30}$$

where λ is the scale factor.

$$M_M^{gyr} = \frac{I_{FS}}{\lambda^5} \omega_{FS} \sqrt{\lambda}\, \Omega_{FS} \sqrt{\lambda} \tag{31}$$

Thus, the rotor angular velocity at model scale should be:

$$\omega_M = \omega_{FS} \sqrt{\lambda} \tag{32}$$

For the 5MW wind turbine (12,1 rpm max rotor speed, scale factor 1:40), this gives:

$$\omega_M = 76{,}5\ rpm \tag{33}$$

Regarding the simulation of the WT aerodynamic loading, flow similarity requires equality of the pertinent Reynold numbers of the air flow, which is not possible for the scale factors considered (taking into account that air viscosity is practically constant, for λ=40 and a full scale wind speed of 10m/s, the scaled airflow speed becomes 400m/s). Under these conditions, only the steady (aerodynamic) thrust can be specified either by means of small thrusters mounted at WT nacelle level, or by a pulling force, applied through a horizontal string, pulley and weight. The first approach was followed in the current work, the model being equipped with two small thrusters installed at the nacelle level, calibrated to produce the required static thrust.

Concluding, it should be mentioned that in order to compare the numerical predictions with the experimental measurements, the aerodynamic loads of the WT, as aforementioned, were taken into consideration assuming steady inflow conditions (i.e. no fluctuations due to turbulence). Since consideration of the unsteady aerodynamic loads of the rotor plays an important role in the dynamic response of a floating wind turbine system, dedicated dynamic analysis of the combined floating system is proposed by the standards in the context of time domain simulations employing the so-called hydro-servo-aero-elastic tools [i.e. hGAST (Riziotis & Voutsinas, 1997; Manolas, Riziotis & Voutsinas, 2014)]. However, this analysis goes beyond the scope of this paper. In this context (frequency domain analysis considering the 6 dofs of the floater), the (reference) forcing term in Eq. (26) includes steady state loading applied to the floater, accounting for aerodynamics, gravity loading of the WT members and inertia due to rotation, and can be used to define the mean static position of the floater. On the other hand, the contribution of the WT to the response of the floater (i.e. caused by the variation of the aerodynamic load or of the gravity moment applied on the floater due to its motion) is inherently taken into account through the added mass, damping and stiffness matrices ($M_{i,j}^{WT}$, $B_{i,j}^{WT}$, $K_{i,j}^{WT}$).

Following the above considerations, an extensive set of experiments were conducted in the wave tank of the Laboratory for Ship and Marine Hydrodynamics (LSMH) of the National Technical University of Athens (NTUA) at a scale of 1:40. A wide range of incident harmonic waves was considered, corresponding to the sea

states that a TLP is expected to encounter in the Aegean Sea (Fig. 8).

The amplitudes of the waves generated by the wave maker of the tank were measured by two standard wire type wave probes, one located near the wave maker and the other in front of the platform.

The motions of the TLP platform subjected to the waves were recorded by an optical system utilising an array of four digital cameras capturing the motion of special optical targets placed at various locations on the platform and on the tower of the wind turbine.

Dynamic pressures inside the air chamber of the OWC device were measured by three pressure transducers, two located on the dome of the chamber of the front cylinder (1st OWC, see Fig. 5), while the third sensing the outside pressure (see Fig. 9).

For the measurement of the water surface level inside the OWC chambers, three wave probes were used, located in the toroidal space of the OWC air chamber, spaced 120^{o} apart (see Fig. 10). The elevation of the internal surface was obtained on the basis of these elevation measurements. Assuming a flat shape for the internal surface and considering also that the motions of the TLP platform are horizontal, due to the large amount of the TLP system pretension, the air volume flux was computed by time differentiating the above measurements, taking into account the area of the OWC net cross section.

A six degrees of freedom (6-dof) of load cell was inserted, between the tower base and the platform (see Fig.

Fig. 8: Scale down model of the platform (scale 1:40).

Fig. 9: Three pressure transducers for the pressure inside the frond cylinder of the OWC device.

Fig. 10: Wave probes inside the OWC air chamber.

Fig. 11: Accelerometers and optical targets for motion recording.

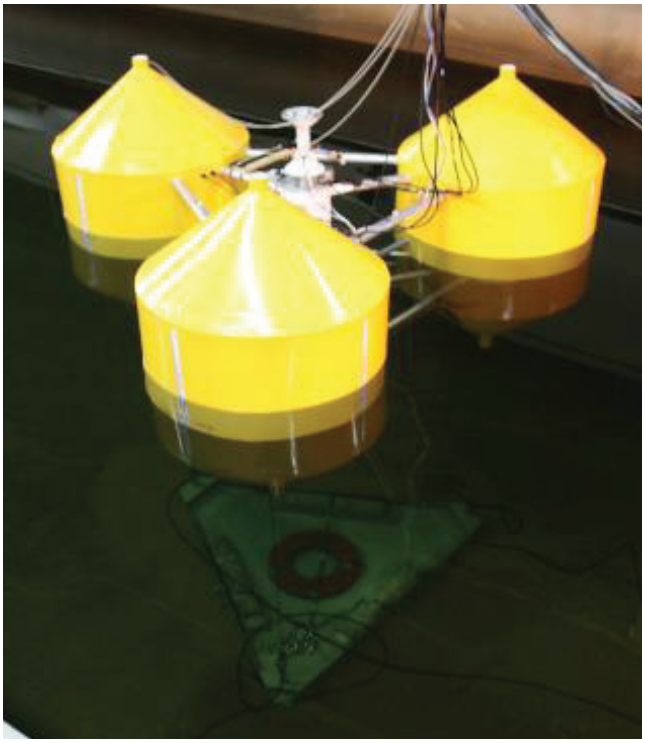

Fig. 12: Base for the TLP mooring system.

11), for the measurement of the inertial loads exerted at this point. Furthermore, the accelerations of the platform were captured by accelerometers mounted on the platform deck, while the static pretension and dynamic tension of the mooring legs was measured by an underwater load cell, installed at the bottom end of each tendon line (Fig. 12).

Experimental Measurements

Hydrodynamic Response

The non-dimensional linear response amplitude operators (RAO's, motion amplitude per unit wave amplitude) for the surge motion of the platform were obtained by measuring the platform motion under the action of monochromatic waves with various frequencies. These are presented in Figures 15 and 22, for various orifice diameters (i.e. 20mm and 40mm), plotted against the numerical predictions, the two investigations being in good agreement.

Figures 15 and 22 also present the response operators for the induced accelerations at the base of the tower of the wind turbine.

Measurement of the OWC Parameters

A Wells turbine is integrated in the full scale concept, for the conversion of air flow energy to electricity. This device is designed for directional changing air flows, like the ones produced by the action of the waves inside the air chamber of the OWC. Since a direct scaling of a specific Wells turbine was outside of the scope of the current study (that does not follow the applied Froude's scaling law), a general bi-directional turbine was assumed for the experimental work, in order to produce the desired air pressure drop. Indeed, the performance of the OWC device is related to the pressure difference (drop) along the device and the volumetric flow rate, passing through the air turbine. The equivalent device consists of a conical chamber cover and an orifice of suitable diameter. The parameters related to the performance of this equivalent device are elaborated below.

In the experimental model presented herein, tests were carried out with 20 and 40mm in diameter orifices, since the effect of the orifice on the pressure depends on the diameter. In general, the effect of a bi-directional turbine is approximated, in pertinent numerical models, by a linearized relationship between the pressure drop and the corresponding volumetric flow rate (Falnes, 2002) (see Eq. 10).

The selection of the Λ value obviously affects the operation of the device; thus, it should be subjected to optimization. Following the orifice approach, an equivalent linearized relationship between pressure drop, Δp, and volumetric flow rate, Q, can be established, by linearising the nonlinear relationship, pertinent to the orifice action. Indeed, the volumetric flow rate is related to the pressure drop by a general equation in the form of (Falnes, 2002):

$$Q = C_f A_0 \sqrt{(\Delta p/\rho)} \tag{34}$$

where ρ the air density A_0 the orifice area and C_f the orifice parameter, usually defined experimentally (Sheng *et al.,* 2012). By solving Δp, the following is obtained:

$$\Delta p = \frac{1}{2}\rho \frac{1}{C_f^2 A_0^2} Q^2 \tag{35}$$

and, by considering bidirectional flows:

$$\Delta p = C_e Q|Q| \tag{36}$$

where C_e is an equivalent coefficient, to be determined experimentally.

In the experimental work, the instantaneous pressure drop was measured by the pressure transducers of

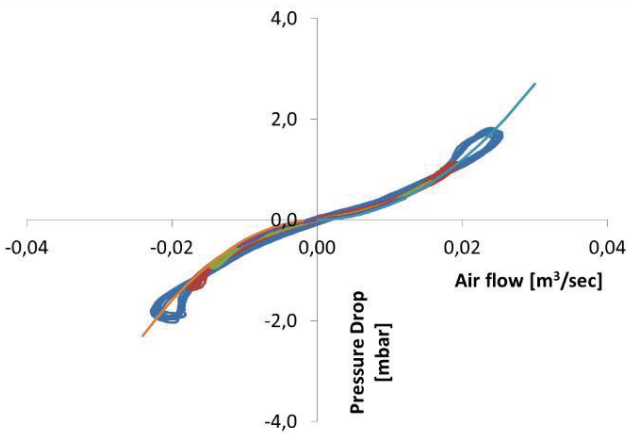

Fig. 13: Pressure drop to flow rate relation, Orifice D=40mm.

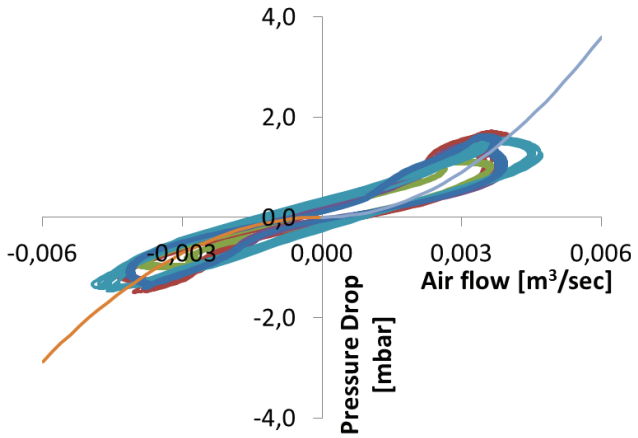

Fig. 14: Pressure drop to flow rate relation, Orifice D=20mm.

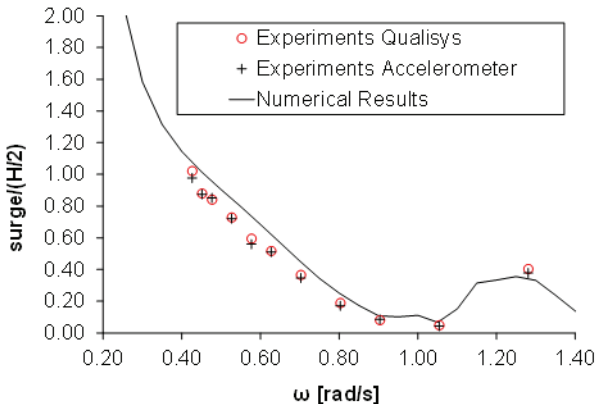

Fig. 15: Surge RAO's comparisons.

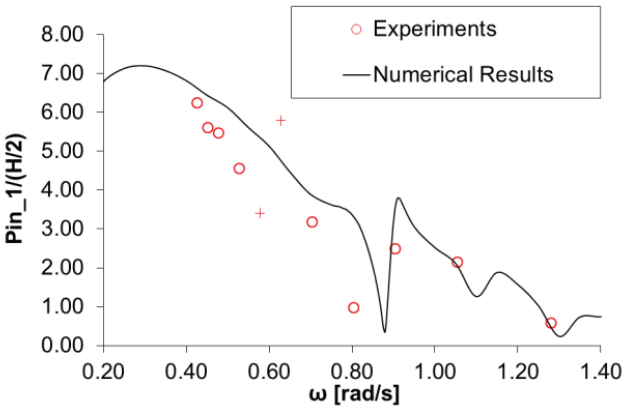

Fig. 16: Air pressure inside the 1st OWC of the platform. Comparisons with experimental results.

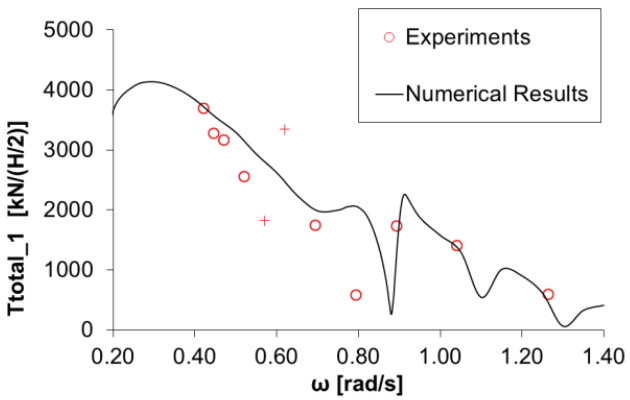

Fig. 17: Mooring tensions comparisons on the 1st OWC.

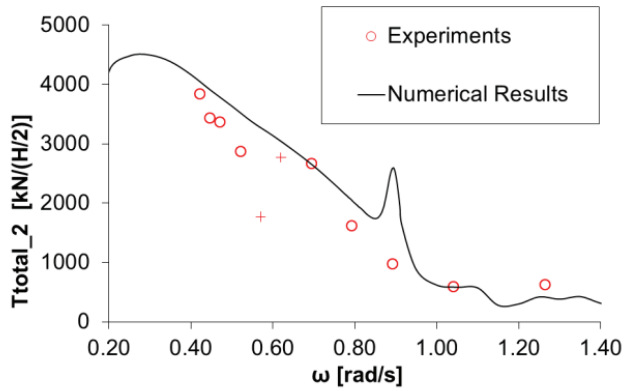

Fig. 18: Mooring tensions comparisons on the 2nd OWC.

the measuring system, while the volumetric flow rate was computed on the basis of the wave probe readings inside the chamber. The instantaneous pressure is plotted against the volumetric flow rate in Figures 13 and 14, in order to obtain the C_e values for orifice diameters 40mm and 20mm, respectively. Many individual curves are over-plotted in the figures, obtained from many experiments, with various wave amplitudes. The nonlinear character of the relationship between the pressure and the flow rate is evident. However, an equivalent linearization can in principle be obtained, by defining a linear regression on a specific range of the pressures, or flows, of interest.

An approximate curve can be fitted to the above experimental data, in the case of the 40mm diameter orifice and for a flow rate of up to 0.026 m³/sec:

Compression phase:

Δp [mbar] = 3 10^3 Q $|Q|$, Q in [m³/sec]

Suction phase:

Δp [mbar] = 4 10^3 Q $|Q|$

Similar curves were also obtained for the other orifice diameter, i.e. 20mm (see Fig. 14).

The pressure drop, plotted against the frequency of the incoming waves, is shown in Figures 16 and 24, for orifice diameters 20mm and 40mm , respectively. The above analysis shows that these diameters (i.e. 20mm and 40mm) correspond to a Λ value of 0.10 kN.sec/m⁵ and 0.02 kN.sec/m⁵, respectively. The pressure drop values are given as linearized RAOs based on tests with harmonic waves of various amplitudes. A scattering of the values can be observed, which could be due to the aforementioned nonlinear character of the orifice equation, which affects the pressure formation.

Dynamic Tension on the Mooring Lines

The dynamic tension exerted on the mooring lines of the TLP platform appears to be dominated by the pressure formation inside the chambers of the OWC devices. In Figures 17-19 and 25-27, the dynamic tension of the

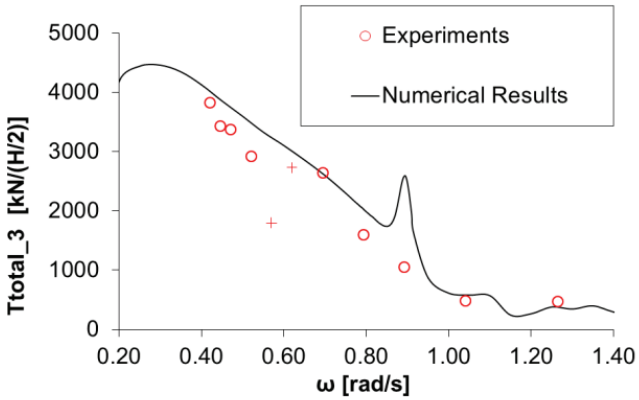

Fig. 19: Mooring tensions comparisons on the 3rd OWC.

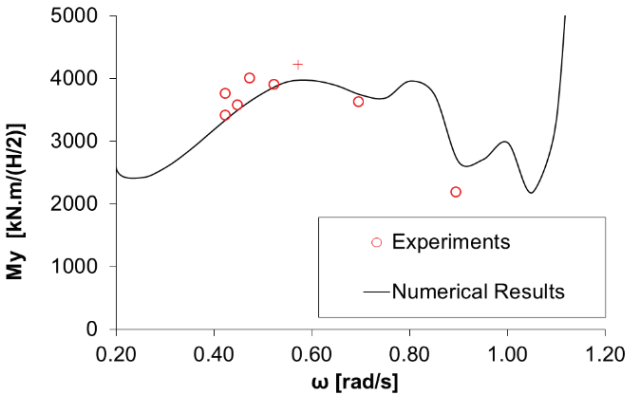

Fig. 21: Shear moments comparisons on the bottom of the WT.

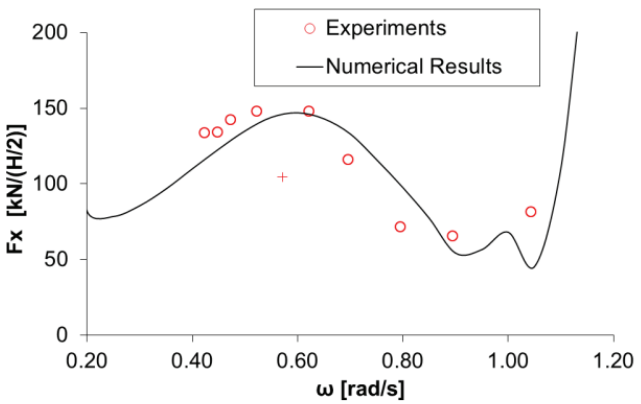

Fig. 20: Comparisons of shear forces at WT base.`

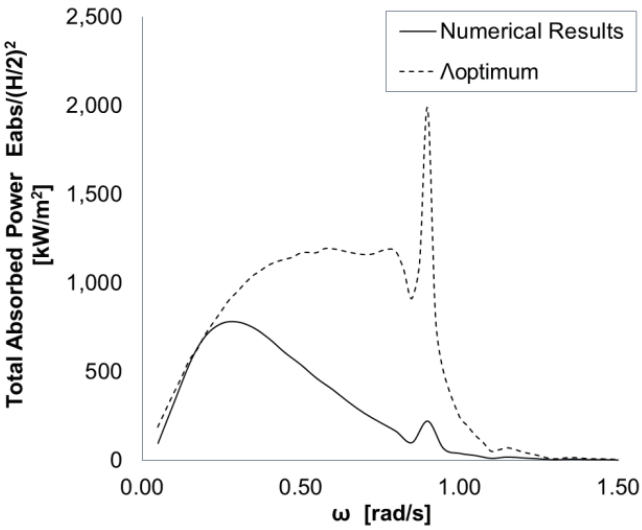

Fig. 22: Total absorbed wave power by the platform for $\Lambda = 0.1$ kN.sec/m^5 and Λ_{opt} coefficients.

mooring lines 1, 2, 3 (see Fig. 5) is presented as linearized RAOs, for every examined orifice diameter. The same observation regarding the scatter of the values can be made here, as in the case of the pressure drop.

Results

Numerical Results & Comparisons with the Experiments

In this section, the Response Amplitude Operators (RAOs) of the surge motion of the platform; the inner air pressure of each OWC device; the dynamic tension exerted on the mooring lines and the shear forces and moments on the WT's tower base are predicted by the numerical analysis. These results are compared with good correlation with the experimental data. Also, the total wave power absorbed by the platform is plotted for the two aforementioned orifice diameters (i.e. two Λ coefficient values) against its theoretical counterpart for the Λ_{opt} value.

The CPU time for each wave frequency related to the overall coupled problem solution (diffraction, motion- and pressure- radiation problem including the WT's contribution to the floater) using HAMVAB software (Mavrakos, 1995) is about 56s.

Orifice diameter 20mm

The surge motion of the moored structure and the air pressure inside the 1st OWC are presented in Figures 15 and 16, respectively, for orifice diameter 20mm. Figures 17-19 present the mooring line tension of the structure and Figures 20 and 21 the shear forces and moments at the WT's tower base. In Figure 22, the platform's total absorbed power Eabs/(H/2)^2 for Λ = 0.1 kN.sec/m^5 is compared against the total absorbed power assuming an air turbine in each air chamber with Λ_{opt} coefficient.

More specifically, Figure 15 presents the calculated non-dimensional linear RAOs for the surge motion of the platform and for the induced accelerations at the base of the tower of the WT. The RAOs of the inner air pressure of the 1st OWC device of the platform are depicted versus the experimental results in Figure 16. It is evident that the air pressure inside the 1st OWC for the array configuration has a peculiar behaviour near ω=0.9 rad/s. This behaviour can be traced back to the well- known resonant fluid motions phenomena inside the annular fluid domain formed between the internal cylinder and the external wall of the

OWC chamber (Silverman & Abramson, 1966; Konispoliatis & Mavrakos, 2016). Furthermore, a local resonance is depicted around ω=0.6 rad/s (see the cross marks in Fig. 16). The latter, following the investigations of the side wall effects on the hydrodynamic characteristics of vertical truncated cylinders placed in a narrow wave tank of Yeung & Sphaier (1989), McIver (1993), Mavrakos & Grigoropoulos, (1994), can be traced back to the symmetric transverse resonant modes that appear in the tank at frequencies corresponding to $kl/2\pi$=1,2,… Here, l is the width of the channel and k the wave number. Considering the width of the experimental wave tank of the NTUA, i.e. l=4.56m, then $\omega\approx$0.58 rad/s for the full scale model (scaling factor 1:40).

The numerical and experimental results for the tensions at Line 1, Line 2 and Line 3 of the TLP platform are given in Figures 17-19. It is depicted that the dynamic tension exerted on the mooring lines seems to be dominated by the pressure generated inside the chambers of OWC devices. The same observation regarding the scatter of the values (i.e. around ω=0.6 rad/s) can also be made here, as in the case of a pressure drop.

The Fx and My shear forces and moments at the bottom of the WT, plotted against the frequency of the incoming waves, are shown in Figures 20 and 21. The values are given as RAOs based on tests with harmonic waves of various amplitudes.

In Figure 22 the total absorbed power for the Λ factor of the specific orifice is compared against the total absorbed power, when assuming optimum Λ factor for the air turbine at each specific frequency. It can be concluded from the figure that at wave frequencies $\omega < 0.25$ and ω>1.2 rad/s the absorbed power for Λ = 0.1 kN.sec/m^5 tends to the absorbed power for an optimum value of Λ. However, this is not the case for the remaining values of wave frequencies where the absorbed power from the structure for the examined orifice (i.e. Λ = 0.1 kN.sec/m^5) is much lower compared to the wave power absorbed by the structure with optimum turbine characteristics.

In order to assess the absorbed wave power, P, by the structure for the examined orifice in irregular sea conditions, the Jonswap spectrum, $S(\omega)$, (DNV, 2007) is applied at indicative environment conditions (H_s, T_p), according to the relation (Cruz *et al.,* 2010):

$$P = \int 2\,\mathrm{Eabs}\,S(\omega)\,d\omega \qquad (37)$$

More specifically, in Table 6, the absorbed power by the structure, P, is presented for indicative pairs of (H_s, T_p).

Orifice diameter 40mm

This section presents the comparisons made between the experimental data and the corresponding numerical results, as mentioned above, for orifice diameter 40mm. More specifically, the surge motion of the platform and the 1st OWC inner air pressure are depicted in Figures 23 and 24, respectively. The tension forces exerted on each mooring line (Line 1, 2, 3) and the shear forces and moments at the bottom of the WT are presented in Figures 25, 26, 27 and 28, 29, respectively. Finally, the platform's total absorbed wave power Eabs/(H/2)^2 for Λ= 0.02 kN.sec/m^5 is compared against the corresponding total absorbed power for Λ_{opt} coefficient in Figure 29.

In addition to the above inferences, it is depicted that the inner pressure and, therefore, the mooring line tension forces, decrease with increasing orifice diameter. Furthermore, a comparison of Figures 15 and 23 reveals that orifice diameter does not affect the surge motion of the platform.

Figure 30 shows that the total power absorbed by the structure, for the examined orifice (i.e. Λ= 0.02 kN.sec/m^5), has higher values, at ω>0.3 rad/s, compared to the total absorbed power for Λ = 0.1 kN.sec/m^5, and tends to the corresponding power absorbed by the structure with optimum turbine characteristics.

Following Eq. (37), the power absorbed by the structure, in irregular wave conditions, is presented in Table 7, for indicative pairs of (H_s, T_p).

Table 6. Absorbed wave power P (kW).

H_s (m)	T_p (s)	P (kW)
1.5	6.5	16.297
2.5	7.5	85.919
3.5	8.5	258.713
4.5	9.5	591.302

Table 7. Absorbed wave power P (kW).

H_s (m)	T_p (s)	P (kW)
1.5	6.5	62.579
2.5	7.5	319.572
3.5	8.5	899.424
4.5	9.5	1879.216

Discussion and Conclusions

A TLP floater supporting the NREL 5MW WT and encompassing three OWC devices has been analysed. Environmental conditions for four possible installation locations in the Aegean Sea have been presented. For the design, the RAOs of the complete system have been calculated using a frequency domain analysis solution, considering the WT's effect on the floater's degrees of freedom after a linearization process based on a ROM model.

Moreover, a scaled-down physical array model of the proposed multi-purpose floating structure was built and an experimental campaign was conducted in order to validate the presented numerical results. The static thrust of the WT was modelled by two thrusters installed at the nacelle level and the OWC's power take off by various orifice diameters producing a similar relationship between the pressure drop and the air flow rate as that of the full scale model, since the modelling of the air turbine

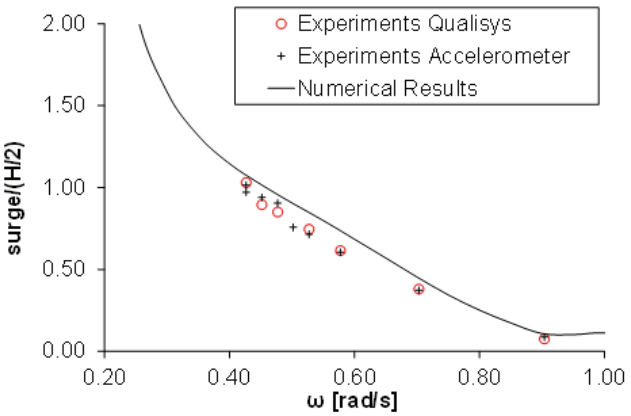

Fig. 23: Surge RAO's comparisons.

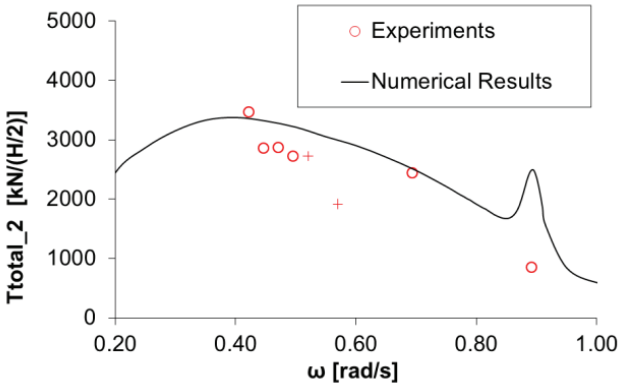

Fig. 26: Mooring tensions comparisons on the 2nd OWC.

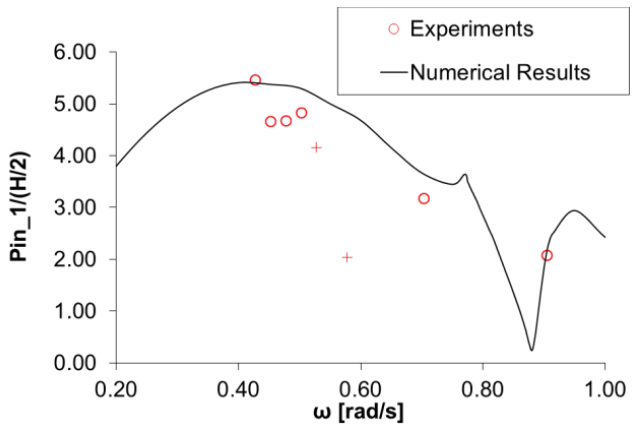

Fig. 24: Air pressure inside the 1st OWC of the platform. Comparisons with experimental results.

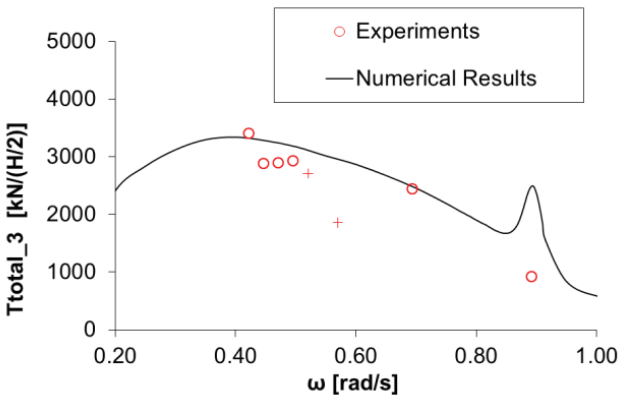

Fig. 27: Mooring tensions comparisons on the 3rd OWC.

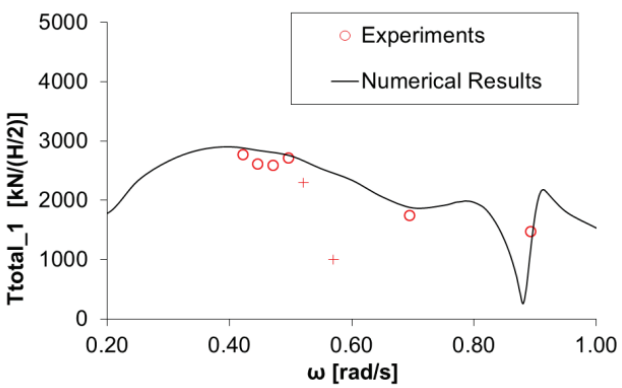

Fig. 25: Mooring tensions comparisons on the 1st OWC.

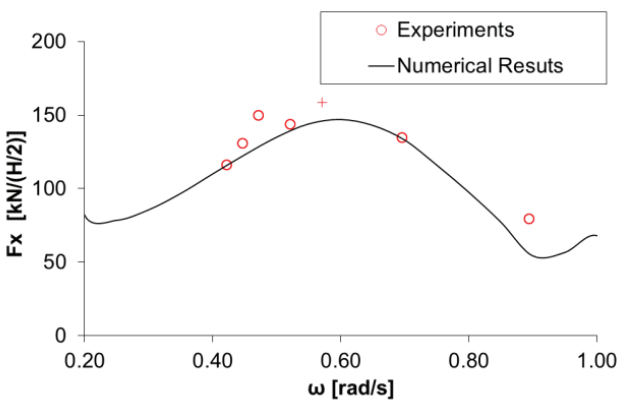

Fig. 28: Comparison of shear forces at the WT base.

was beyond the scope of the current study. However the nonlinearities in the relationship between the pressure and the flow rate are evident. In the proposed numerical simulations, an equivalent linearization can be obtained in principle, by defining a linear regression for a specific range of the pressures, or flows, of interest.

From the analysis carried out within the framework of the research study, the following conclusions can be drawn:

1. The responses of the platform have been well-predicted. The orifice sizes have little influence on the horizontal motions of the structure because, as mentioned by Mavrakos & Konispoliatis (2012) for an isolated device, only the heave motion affects the volumetric oscillations in evaluating the volume flow.
2. Tension forces along the mooring tendons and air pressures inside the OWCs are very dependent on orifice diameter, i.e. on the Λ parameter of the OWC turbine, with the larger values of tension and pressure corresponding to large Λ parameters.
3. A general good agreement between the numerical and experimental results was observed. Apart from the frequency ranges where both the methods

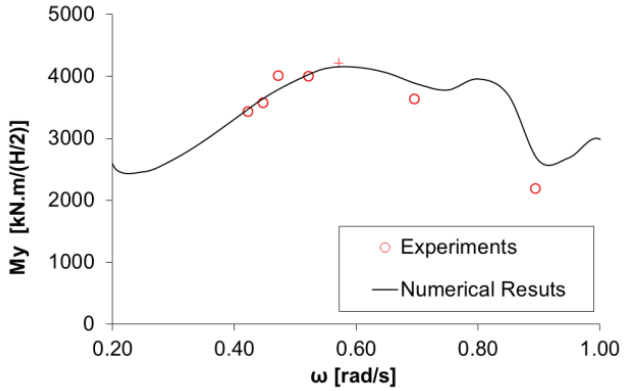

Fig. 29: Shear moments comparisons on the bottom of the WT.

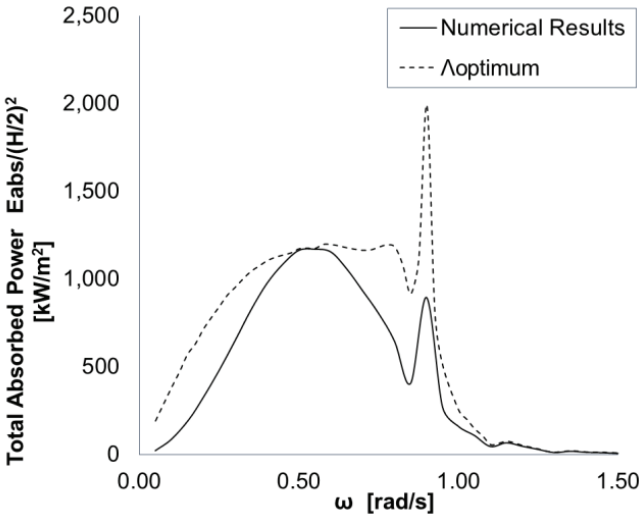

Fig. 30: Total absorbed wave power by the platform for Λ = 0.02 kN.sec/m^5 and Λ_{opt} coefficients.

produced similar results, there were two distinct frequency areas where the results showed a peculiar behaviour, namely near 0.9 and 0.6 rad/sec. The first area was depicted by both the numerical and experimental methods and corresponds to the occurrence of resonant fluid motion phenomena of the water trapped between the internal cylinder and the outer wall of the OWC's chamber. The second one, depicted only in the experimental results, can be traced back to the effects of the side walls in a narrow experimental tank.

4. The platform's absorbed power for orifice diameter 40mm tends to the corresponding values of Λ_{opt}. On the other hand, for orifice diameter 20mm the values of absorbed power are lower than those obtained with optimum turbine coefficients. To conclude, the power production performance of OWCs are closely affected by the characteristics of the air turbines inside the oscillating chambers. Representative values of the OWC energy yield for particular pairs of (H_s, T_p) are given in Tables 6 and 7. The wave power yield of OWCs contributes to the total absorbed power (i.e. wind and wave), thus increasing the power output of the multi-purpose floating structure. This increases the efficiency of the entire system due to the fact that the absorbed wave power can cover the construction cost of the WT during its life cycle.

Acknowledgement

This research was co-financed by the European Union (European Social Fund-ESF) and Greek national funds through the Operational Program "Education and Lifelong Learning" of the National Strategic Reference Framework (NSRF) 2007-2013: Research Funding Program: ARISTEIA, Program POSEIDON (2041).

References

Aubault, A., Alves, M., Sarmento, A. Roddier, D., Peiffer, A., 2011. Modeling of an oscillating water column on the floating foundation WINDFLOAT. In: *30th International Conference on Offshore Mechanics and Arctic Engineering, OMAE 2012, 19 – 24 June 2011,* Rotterdam, The Netherlands.

Baarholm, G.S., Haver, S., Økland, O.D., 2010. Combining contours of significant wave height and peak period with platform response distributions for predicting design response, *Marine Structures*, 23 (2), 147-163.

Black, J.L., Mei, C.C., Bray, M.C.G., 1971. Radiation and scattering of water waves by rigid bodies. *Journal of Fluid Mechanics,* 46, 151-164.

Cheng, P. W., van Bussel, G.J.W., van Kuik, G.A.M., Vugts, J.H., 2003, Reliability-based Design Methods to Determine the Extreme Response Distribution of Offshore Wind Turbines. *Wind Energy*, 6 (1), 1-22.

Coleman, R.P., 1943. Theory of self-excited mechanical oscillations of hinged rotor blades. *Technical Report NACA-WR-L-308, Langley Research Center*, available from ntrs.nasa.gov.

Cruz, J., Sykes, R., Siddorn, P., Taylor, R.E., 2010, Estimating the Loads and Energy Yield of Arrays of Wave Energy Converters under Realistic Seas. *IET Renewable Power Generation,* 4 (6), 488-497.

Delaure, Y.M.C., Lewis, A., 2003. 3D Hydrodynamic modeling of fixed oscillating wave power plant by a Boundary Element Method. *Ocean Eng*ineering, 30, 309-330.

DNV, 2007, Environmental Conditions and Environmental Loads, Recommended Practice DNV-RP-C205.

Evans, D.V., Porter, R., 1996. Efficient calculation of hydrodynamic properties of O.W.C type devices. *Journal of Offshore Mechanics and Arctic Engineering,* 119 (4), 210-218.

Falcao, A.F. de O., 2002. Wave power absorption by a periodic linear array of oscillating water columns. *Ocean Eng*ineering, 29, 1163-1186.

Falnes, J., McIver, P., 1985. Surface wave interactions with systems of oscillating bodies and pressure distributions. *Applied Ocean Research*, 7, 225-234.

Falnes, J., 2002. *Ocean Waves and Oscillating Systems*, Cambridge University Press, Cambridge, U.K.

Garrett, C.J.R., 1971. Wave forces on a circular dock. *Journal*

of Fluid Mechanics, 46 (1), 129-139.

Kagemoto, H., Yue, D.K.P., 1986. Interactions among multiple three-dimensional bodies in water waves: an exact algebric method. *Journal of Fluid Mechanics,* 166, 189-209.

Katsaounis, G.M., Polyzos, S., Mavrakos, S.A., 2017. An experimental study of the hydrodynamic behavior of a TLP platform for a 5MW Wind Turbine with OWC devices. In: *The VII International Conference on Computational Methods in Marine Engineering (MARINE 2017), 15-17 May 2017*, Nantes, France.

Kokkinowrachos, K., Thanos, I., Zibell, H.G., 1987. Hydrodynamic analysis of some wave energy conversion systems. In: *The OCEANS'87 Conference*. Halifax, Canada, 566-574.

Konispoliatis, D.N., Mavrakos, S.A., 2016. Hydrodynamic analysis of an array of interacting free-floating oscillating water column devices. *Ocean Engineering,* 111, 179-197.

Konispoliatis, D.N., Mazarakos, T.P., Mavrakos S.A., 2016. Hydrodynamic analysis of three-unit arrays of floating annular oscillating-water-column wave energy converters. *Applied Ocean Research*, 61, 42-64.

Li, L., Gao, Z., Moan, T., 2013. Joint Environmental Data At Five European Offshore Sites For Design Of Combined Wind And Wave Energy Devices. In: *The 32nd International Conference on Ocean, Offshore and Arctic Engineering, OMAE2013-10156, 9-14 June 2013*, Nantes, France.

Manolas, D.I., Riziotis, V.A., Voutsinas, S.G., 2014. Assessing the importance of geometric non-linear effects in the prediction of wind turbine blade loads. *Computational and Nonlinear Dynamics Journal,* 10, 041008.

Martins-rivas, H., Mei, C.C., 2009. Wave power extraction from an oscillating water column at the tip of a breakwater. *Journal of Fluid Mechanics,* 626, 395-414.

Mavrakos, S.A, Koumoutsakos, P., 1987. Hydrodynamic interaction among vertical axisymmetric bodies restrained in waves. *Applied Ocean Research,* 9 (3), 128-140.

Mavrakos, S.A., 1991. Hydrodynamic coefficients for groups of interacting vertical axisymmetric bodies. *Ocean Engineering*, 18 (5), 485-515.

Mavrakos, S.A., Grigoropoulos, G.J., 1994. Numerical and experimental investigation of the exciting wave loads on a vertical truncated cylinder. In: *5th International Conference of Hydraulic Engineering Software*, *(HYDROSOFT 94)*.

Mavrakos, S.A., 1995. Users Manual for the Software HAMV-AB, School of Naval Architecture and Marine Engineering, Laboratory for Floating Structures and Mooring Systems, Athens, Greece.

Mavrakos, S.A., McIver, P., 1997. Comparison of methods for computing hydro-dynamic characteristics of array of wave power devices. *Applied Ocean Research*, 19, 283-291.

Mavrakos, S.A., Konispoliatis, D.N., 2012. Hydrodynamics of a free floating vertical axisymmetric oscillating water column device. *Hindawi Publishing Corporations Journal of Applied Mathematics, Mathematical Modelling of Marine Structures*, Vol.2012; Article ID 142850.

Mazarakos, T.P., Mavrakos, S.A., Konispoliatis, D.N., Voutsinas, S., Manolas, D., 2014. Frequency domain analysis for a coupled hydro-aero-elastic behavior of a moored multi-purpose floating structure. In: *COCONET Workshop for Offshore Wind Farms in the Mediterranean and Black Seas*, *Hellenic Center of Marine Research*, Anavyssos, Greece, 2014.

Mazarakos, T.P., Konispoliatis, D.N., Manolas, D., Voutsinas, S., Mavrakos, S.A., 2015. Modelling of an offshore multi-purpose floating structure supporting a wind turbine including second-order wave loads. In: *The 11th Eur. Wave & Tidal Energy Conf*, *6-11 September 2015*, Nantes, France.

Mazarakos, T.P., Konispoliatis, D.N., Katsaounis, G., Polyzos, P., Manolas, D. *et al.,* 2017. Numerical and experimental studies of an offshore multi-purpose floating structure supporting a wind turbine. In: *The 12th Eur. Wave & Tidal Energy Conf*, *27 August - 1 September 2017*, Cork, Ireland.

Mazarakos, T.P., Konispoliatis, Mavrakos, S.A., 2018. Loads on the brace system of an offshore floating structure. *The 13th International Marine Design Conference*, *10-14 June 2018*, Helsinki, Finland.

McIver, P., 1993. The wave field scattered by a vertical cylinder in a narrow wave tank. *Applied Ocean Research*, 15, 25-37.

Miles, J., Gilbert, F., 1968. Scattering of gravity waves by a circular dock. *Journal of Fluid Mechanics*, 34 (4), 783-793.

Okhusu, M., 1974. Hydrodynamic forces on multiple cylinders in waves. University College London, London. In: *Int. Symposium on the Dynamics of Marine Vehicles and structures in Waves*.

Papadopoulos, A., Katsafados, P., 2009. Verification of operational weather forecasts from the POSEIDON system across the Eastern Mediterranean. *Natural Hazards and Earth System Sciences*, 9, 1299-1306.

Papadopoulos, A., Korres, G., Katsafados, P., Ballas, D., Perivoliotis, L. *et al.*, 2011. Dynamic downscaling of the ERA-40 data using a mesoscale meteorological model. *Mediterranean Marine Science,* 12, 183-198.

Riziotis, V.A., Voutsinas, S.G. 1997. GAST: A general aero-dynamic and structural prediction tool for wind turbines. In: *The European Wind Energy Conference 1997*, Dublín, Ireland, 1997. Rasmussen F. Identification of structural.

Rosenblatt, M., 1952. Remarks on a multivariate transformation. *The Annals of Mathematical Statistics*, 23 (3), 470-472.

Sheng, W., Flannery, B., Lewis, A., Alcorn, R., 2012. Experimental studies of a floating cylindrical OWC WEC. In: *31st International Conference on Offshore Mechanics and Arctic Engineering, OMAE 2012*, *1 - 6 July 2012,* Rio de Janeiro, Brazil.

Siddorn, P., Eatock Taylor, R., 2008. Diffraction and independent radiation by an array of floating cylinders. *Ocean Engineering*, 35, 1289-1303.

Silverman, S., Abramson, N., 1966. Lateral sloshing in moving containers. The Dynamic Behavior of Liquids in Moving Containers. NASA SP-106, edited by Norman H. Abramson, 467 pages, published by NASA, Washington, D.C.

Soukissian, T.H., Chronis G. Th., 2000. POSEIDON: A marine environmental, monitoring, forecasting and information system for the Greek Seas. *Mediterranean Marine Science*, 1 (1), 71-78.

Soukissian, T.H., G. Kalantzi, 2006, "Extreme value analysis methods used for wave prediction", In: *16th International Offshore and Polar Engineering Conference, 28 May - 2 June 2006,* Vol. III, 10-17, ISBN 1-880653-66−4, San Francisco, California.

Soukissian, T.H., Kalantzi, G., 2007. A new method for apply-

ing the r-largest maxima model for design sea-state prediction", *Proceedings of the 17th International Offshore and Polar Engineering Conference, Vol. III*, pp. 1843-1849.

Soukissian, T.H., Prospathopoulos, A., Diamanti, C., 2002. Wind and wave data analysis of the Aegean Sea. Preliminary results. *Journal of Atmospheric and Ocean Science*, 8 (2-3), 163-189.

Soukissian, T.H., Prospathopoulos, A., Korres, G., Papadopoulos, A., Hatzinaki, M. *et al.,* 2008. A New Wind and Wave Atlas of the Hellenic Seas. In: *27th International Conference on Offshore Mechanics and Arctic Engineering, OMAE 2008*, June 15-20, 2008, Estoril, Portugal.

Soukissian, T.H., Tsalis, C., 2015. The effect of the generalized extreme value distribution parameter estimation methods in extreme wind speed prediction. *Natural Hazards and Earth System Sciences*, 78, 1777-1809, Springer Netherlands.

Soukissian, T.H., Denaxa, D., Karathanasi, F., Prospathopoulos, A., Sarantakos, K. *et al.,* 2017. Marine Renewable Energy in the Mediterranean Sea: Status and Perspectives. *Energies*, 10 (1512).

Soukissian, T.H., Tsalis, C., 2018. Effects of parameter estimation method and sample size in metocean design conditions. *Ocean Engineering*, 169, 19-37.

Sykes, R.K. Lewis, A.W., Thomas, G.P., 2007. A physical and numerical study of a fixed cylindrical OWC of finite wall thickness. *The 7th Eur. Wave & Tidal Energy Conf, 11-13 September 2007*, Porto, Portugal.

Twersky, V., 1952. Multiple scattering of radiation by an arbitrary configuration of parallel cylinders. *Journal of the Acoustical Society of America,* 24 (No.1).

Yang, X., Chang, Q., 2013. Joint probability distribution of winds and waves from wave simulation of 20 years (1989-2008) in Bohai Bay, Water Science and Engineering, 6 (3), 296-307.

Yeung, R.W., Sphaier, S.H., 1989. Wave-interference effects on a truncated cylinder in a channel. Journal of Engineering Mathematics, 23, 95-117.